

High-Resolution Simulations of Cluster Formation

Tereasa G. Brainerd¹, David M. Goldberg² & Jens Verner Villumsen³

¹*Boston University, Dept. of Astronomy, 725 Commonwealth Ave., Boston, MA 02215*

²*Princeton University, Dept. of Astrophysical Science, Peyton Hall, Princeton, NJ 08544*

³*Max-Planck-Institut für Astrophysik, Karl-Schwarzschild-Strasse 1, 85740 Garching bei München, Germany*

ABSTRACT

The formation history of rich clusters is investigated using a hybrid N-body simulation in which high spatial and mass resolution can be achieved self-consistently within a small region of a very large volume. The evolution of three massive clusters is studied via mass accretion, spherically-averaged density profiles, three-dimensional and projected shapes, and degree of substructure. Each cluster consists of $\sim 4 \times 10^5$ particles at the present epoch and in the case that rich cluster evolution is well-described by a 1-parameter family, the simulations have sufficient resolution to demonstrate this. At $z = 0$ the clusters have similar masses, $M(r \leq 1.5h^{-1}\text{Mpc}) \sim 2 \times 10^{15}h^{-1}M_{\odot}$, and similar spherically-averaged density profiles, however markedly different formation histories are observed. No single, dominant pattern is apparent in the time variation of the mass accretion rate, the cluster shape, or the degree of substructure. Although not a statistically large sample, these objects suggest that the detailed formation history of rich clusters cannot be characterized by a simple 1-parameter family. These results suggest that the use of observations of rich clusters over a wide range of redshifts to constrain cosmological parameters may not be entirely straightforward.

Subject headings: cosmology: dark matter — cosmology: large-scale structure of the universe — cosmology: theory — methods: numerical

Submitted to *The Astrophysical Journal*, June 1997

1. INTRODUCTION

The evolution history of clusters of galaxies is a potentially powerful constraint on theories of the formation of large-scale structure in the universe. Although a statistically large sample does not yet exist, it is possible to identify clusters to high redshift (eg. Smail & Dickinson 1995; Bower & Smail 1997; Deltorn et al. 1997; Luppino & Kaiser 1997; Steidel et al. 1997) and it is hoped that eventually a complete description of the time evolution of these objects will be obtained. Additionally, detailed studies of clusters have yielded evidence for significant amounts of substructure in many clusters, even those which appear smooth and round in projection (eg. Beers & Geller, 1983; Jones & Forman 1984; Dressler & Shectman 1988; West & Bothun 1990; Davis & Mushotzky 1993; Miyaji et al. 1993; Mushotzky 1993; White, Briel & Henry 1993; Bird 1994a,b; Zabludoff & Zaritsky 1995). Optical, X-ray, and kinematic evidence has been found for recent mergers of a number of clusters with smaller systems. It appears that at least one third of all clusters are not fully relaxed systems and it is possible that many clusters are still in the process of assembling even today. The fraction of clusters containing significant amounts of substructure at the present epoch is a potentially powerful constraint on the value of the density parameter (eg. Richstone, Loeb & Turner 1992; Bartelmann, Ehlers & Schneider 1993; Kauffmann & White 1993; Lacey & Cole 1993; Mohr et al. 1995) and, therefore, cluster substructure investigations are of considerable interest.

It has been hoped that numerical simulations of cluster formation would provide useful constraints on large-scale structure theories via comparisons of the formation histories of simulated clusters and the observed cluster population. Direct comparisons are, however, problematical for a number of reasons. First, pure N-body simulations follow only the evolution of the dominant, dissipationless mass component of the universe, neglecting hydrodynamics. In such simulations a direct comparison of a theoretical distribution of light (eg. galaxies and X-ray gas) to that of observed clusters is not possible. Under the assumption that density peaks of an appropriate mass scale correspond to the likely sites of galaxy formation, however, it is possible to locate groups of particles within the simulations that may be associated fairly with the dark matter halos of individual galaxies. Additionally, from studies of the coherent weak shear field associated with gravitational lens clusters, the mass of the clusters is certainly dominated by dark matter and in addition it appears that the mass distribution within the clusters traces the smoothed light distribution quite well (eg. Bonnet, Mellier & Fort 1994; Fahlman et al. 1994; Smail et al. 1995; Kneib et al. 1996; Seitz et al. 1996; Squires et al. 1996ab; Smail et al. 1997). Therefore, cluster simulations which include only a dark matter component should yield fairly reasonable results for comparison with observation, at least to a good first approximation.

The worst problem to plague simulations of cluster formation is simply one of resolution, both in terms of the gravitational force calculation on small scales as well as the mass per particle. That is, within the cluster environment itself, one would like to resolve the physical scales associated with galaxies (distances of order a few tens of kiloparsecs, using a mass per particle of order $10^9 M_\odot$). Ideally, of course, one would like to achieve such resolution inside a simulation volume which is itself a “fair sample” of the universe (of order $10^7 h^{-3} \text{Mpc}^3$). Current computing platforms, however, do not allow such a high level of resolution throughout a large simulation volume.

Therefore, high-resolution simulations of cluster formation often follow a scenario in which a simulation of a large volume of the universe is first run at moderate resolution. The final timestep of this simulation is then searched for peaks in the smoothed mass density which would correspond fairly to clusters of galaxies. A sphere of a given radius (typically $r \sim 10h^{-1}$ Mpc) centered on the peak is then excised from the initial conditions of the simulation and populated with a large number of particles of small (sub-galactic) mass (eg. Bromley et al., 1995; Carlberg, 1994). These smaller peak particles are then evolved from the initial timestep to the present epoch, subject to an external potential which is intended to model the correct tidal field due to the local universe that the cluster would experience as it evolves. Difficulties with such simulations are insuring: (1) the radius of the sphere is large enough to include all the mass that should be accreted by the cluster up to the present epoch and (2) the model external potential fairly represents the actual tidal field the cluster would experience if one simply ran the entire simulation at an unachieveably high resolution level.

Here we simulate the formation of 3 rich clusters at very high resolution and investigate the similarities and differences of their evolution histories. All three clusters have similar masses at the present day and for simplicity a standard cold dark matter universe is adopted. The clusters form inside a large computational volume ($8.0 \times 10^6 h^{-1} \text{Mpc}^3$) and high resolution is achieved without the use of either constrained initial conditions or the excision of peaks from a large-scale density field. Instead, a hybrid N-body code utilized. This particular code allows high spatial and mass resolution to be achieved simultaneously within small selected regions of a very large primary simulation volume. High resolution is obtained by nesting small simulations self-consistently inside larger simulations, resulting in a “power zoom” effect. The basic premise behind the N-body code used for the investigation is outlined in §2. Details of the simulations performed are summarized in §3, results of the analysis of the simulations are presented in §4, and a discussion of the results is given in §5.

2. HIERARCHICAL PARTICLE MESH (HPM)

The code used to run the simulations is the Hierarchical Particle Mesh (HPM) code written by J. V. Villumsen (Villumsen, 1989). The heart of the HPM code is a standard particle mesh (PM) cosmological simulation in which mass density is assigned to a grid using a cloud-in-cell (CIC) weighting scheme and Poisson’s equation is solved using fast Fourier techniques. Although very fast, PM simulations suffer from limited spatial resolution, the force being softer than Newtonian on scales smaller than about 2 grid cells. In order to gain both spatial and mass resolution in a small region of the primary simulation volume, the HPM code allows small simulations (“subgrids”) to be nested self-consistently within the main simulation. By nesting subgrids inside subgrids one can progressively build up to very high resolution in a limited region of the total simulation volume. Details of the force calculations and the generation of initial conditions for multi-grid simulations are given in Villumsen (1989); here we present only a brief outline of the premise behind HPM.

It is important to note that a multi-grid simulation using HPM is an *iterative* process. To begin, an ordinary PM simulation of a large volume of the universe is run from the

desired starting epoch ($z \sim 30$) to the present epoch. Periodic boundary conditions are imposed on this grid and the simulation is carried out in a manner similar to all conventional PM simulations of the formation of large-scale structure. Throughout, this large grid shall be referred to as the “top grid”; it constitutes the fundamental computational volume of the simulation.

A small region of interest which is to be run in high resolution mode (eg. a cluster environment) is then selected from the *final timestep* of the top grid. Using the previously recorded timesteps of the top grid calculation, those top grid particles which pass through the region of interest (plus a generous buffer zone) at any time during the course of the simulation are tagged. The entire simulation is then reeled back to the uniform grid stage and for each of the top grid particles that were tagged as having passed through the region of interest, a set of smaller particles is generated for the subgrid calculation. This is done in the following manner. Each of the tagged top grid particles defines a cubical box of length l_t , equal to the interparticle spacing in the top grid. Allowing the subgrid to be a factor of f smaller than the top grid, a virtual grid of subgrid particles is then generated with a spacing of $l_s = l_t/f$ and any virtual particle in a box defined by a top grid particle is counted as a subgrid particle. At this point the subgrid particles constitute a uniform grid which is fully sampled inside the subgrid volume and only partially sampled outside it. Initial conditions for *both* the top grid and the subgrid are then generated by perturbing the top grid and subgrid particles away from their respective uniform grids. (Seeds identical to the seeds used to generate the first set of top grid initial conditions are used so that the initial conditions for the top grid in the multi-grid calculation will be identical to the initial conditions for the top grid alone.)

The full multi-grid calculation is then run with the two sets of initial conditions, the top grid and the subgrid being evolved forward in time simultaneously. The important points to note are: (1) there is no “back-reaction” from the subgrid to the top grid (i.e. the top grid simulation runs completely unaware of the subgrid simulation), (2) the potential in the subgrid is computed using both the small particles in the subgrid and the potential from the top grid (i.e. the force field from the top grid acts as an external field on the subgrid simulation), and (3) unlike the top grid, the subgrid utilizes isolated boundary conditions so that subgrid particles may enter and exit the subgrid region over the course of the simulation. Additionally, the subgrids may either be kept stationary throughout the course of the simulation or they may be allowed to move (eg. to follow the growth of an object which has a large streaming velocity).

An HPM simulation is constrained to use the same number of grid cells in both the top grid and subgrid simulations. Therefore by using a subgrid which is factor of f smaller than the top grid, the gain in spatial resolution in the subgrid region is necessarily a factor of f . The total number of particles used in the subgrid may, however, vary from that used in the top grid. Allowing an identical number of top grid and subgrid particles across a uniform grid, a subgrid which is a factor of f smaller than the top grid results in a mass per particle that is a factor of f^3 smaller than in the top grid. However, in a high density region of the simulation (eg. a cluster) it is oftentimes necessary to reduce the number of uniform grid particles in the subgrid compared to that of the top grid in order to remain within the available machine memory.

Very high resolution in an HPM simulation may be obtained by further nesting subgrids within subgrids. Again, this is an iterative process. At the end of a two-level (top grid plus one subgrid) calculation, a region of interest is identified within the subgrid. All of the subgrid particles which pass through that region of interest over the course of the simulation are tagged and the entire simulation (top grid plus subgrid) is reeled back to the uniform grid stage whereupon a second subgrid is generated within the first subgrid utilizing all the tagged particles from subgrid #1. Using the same random number generator seeds as were used previously, initial conditions for each of the grids (top grid plus two subgrids) are generated by perturbing each of the three sets of particles away from their respective uniform grids. Again, in the multi-grid calculation the grids are evolved forward in time simultaneously, there is no back-reaction from “parent” grid to “child” grid, and the force field from the “parent” grid acts as an external field for the force calculation in the “child” grid.

Since the “child” particles experience high frequency power in their subgrid that their “parent” particles do not, the “child” particles will not move exactly in concert with their “parent” particles. However, the “child” particles do not stray very far from the general location of the “parent” since the extra high frequency power does not induce large streaming velocities. Should a “parent” particle exit/enter the region of a subgrid, it takes its “children” out of/into the region in a smooth manner. A simple consistency check involves comparing the number of “child” particles found inside a given subgrid at a particular time to the number of “parent” particles also within the subgrid at the same time. The ratio of these numbers should be of order the cube root of the ratio of the particle masses in the two grids (but will not be exactly equal to this value owing to the smooth manner in which the “child” particles enter and exit the subgrids). This is, indeed, the case and for the simulations presented here the ratio of the number of “child” particles to “parent” particles differs from the cube root of the ratio of the particle masses by an average of about 6%.

Visual comparisons between the structures in “parent” and “child” grids show excellent agreement (see Fig. 1). However, due to the higher force resolution in the “child” grid, structures in the “child” grid tend to be more concentrated than the analogous, more poorly resolved structures in the “parent” grid. That is, the force in the “child” grid is not as soft as in the “parent” grid, allowing structures to collapse on smaller scales.

3. THE SIMULATIONS

Three multi-grid simulations of the formation of clusters in a standard CDM universe ($H_0 = 50$ km/s/Mpc, $\Omega_0 = 1$, $\Lambda = 0$) were run. All simulations consisted of 3-level calculations: a top grid of length $L_{\text{top}} = 200h^{-1}$ Mpc, inside which was nested a subgrid of length $L_{\text{sub1}} = 33.3h^{-1}$ Mpc, inside which was nested a subgrid of length $L_{\text{sub2}} = 8.3h^{-1}$ Mpc (comoving lengths). In all cases 256^3 grid cells were used, resulting in a grid cell length of $32.6h^{-1}$ kpc (comoving) in the smallest, highest resolution subgrid. A total of 128^3 particles were used in the top grid calculation, resulting in a mass per particle in the top grid of $1.06 \times 10^{12}h^{-1}M_\odot$. Owing to machine memory limitations, the uniform subgrids were constrained to fewer particles than the top grid. The particle mass in the low-resolution subgrids (subgrid #1) was $3.90 \times 10^{10}h^{-1}M_\odot$ while in the high-resolution

subgrids (subgrid #2) it was $4.88 \times 10^9 h^{-1} M_\odot$. At the end of the simulation there were 8.3×10^5 particles inside the high-resolution subgrid containing cluster 1, corresponding to a density of 179 particles per cubic megaparsec. For cluster 2, there were 7.3×10^5 particles inside its high-resolution subgrid at the end of the simulation, corresponding to a density of 159 particles per cubic megaparsec. For cluster 3, there were 9.8×10^5 particles inside its high-resolution subgrid at the end of the simulation, corresponding to a density of 211 particles per cubic megaparsec.

The locations of the subgrids were specified as follows. To begin, a top grid simulation was evolved from $\sigma_8 = 0.033$ to $\sigma_8 = 1.0$, where

$$\sigma_8 \equiv \left\langle \left[\frac{\delta\rho}{\rho}(8h^{-1}\text{Mpc}) \right]^2 \right\rangle^{\frac{1}{2}} \quad (1)$$

Identifying the final timestep of the top grid simulation as the present epoch (redshift, z , of 0), the simulation began at $z = 29$. This is a model which is somewhat under-normalized compared to the COBE observations (eg. Bunn & White 1997) and over-normalized compared to the abundance of rich clusters (eg. Bahcall & Cen 1993; White, Efstathiou & Frenk 1993; Eke, Cole & Frenk 1996; Viana & Liddle 1996). To determine the present-day locations of rich clusters, the mass density field of the top grid at $\sigma_8 = 1.0$ was smoothed with a Gaussian filter of length $1.5h^{-1}$ Mpc and the locations of peaks determined. From this smoothed density field the locations of three of the largest density peaks were selected as the centers of the first subgrids. For each of these subgrids, the top grid particles that passed through the subgrid region (plus 20% buffer zones) were tagged, the simulations were reeled back to the uniform grid stage, initial conditions for 2-level calculations were generated, and the 2-grid simulations were then evolved from $\sigma_8 = 0.033$ to $\sigma_8 = 1.0$. The second, highest resolution subgrids were then chosen to be centered on the centers of mass of the clusters that formed in each of the first subgrids. Again, using the timesteps of the 2-level calculations, the particles in the first subgrids that passed through the regions of the second subgrids (plus buffer zones) were tagged, the simulations were reeled back to the uniform grid stage, initial conditions for 3-level calculations were generated, and the 3-grid simulations were then evolved from $\sigma_8 = 0.033$ to $\sigma_8 = 1.0$.

The clusters investigated here correspond to the very largest (i.e. most massive) of these objects that would typically form in CDM universes. They do not, therefore, represent an unbiased, ‘‘average’’ sample of clusters but may correspond fairly with the ‘‘richest’’ clusters that would form in such universes. Tables 1, 2, and 3 contain summaries of various properties of the clusters obtained from analyses of the highest resolution subgrids. At the end of the simulation all three clusters have masses of order $2 \times 10^{15} h^{-1} M_\odot$ within the Abell radius ($1.5h^{-1}$ Mpc), corresponding to of order 4×10^5 particles in the highest resolution subgrids.

Shown in Fig. 1 are grey-scale pictures of the clusters at $\sigma_8 = 1.0$. The level of grey indicates the logarithm of the mass density along the line of sight in the projection and each projection has dimensions $8.3h^{-1}\text{Mpc} \times 8.3h^{-1}\text{Mpc} \times 8.3h^{-1}\text{Mpc}$. That is, shown in Fig. 1 is a 2-dimensional compression of a 3-dimensional volume corresponding to the full volume of the highest resolution subgrid and each projection is centered on the center of

mass of the cluster. The top panels show the clusters at highest resolution (subgrid #2) and the center panels show the clusters at lower resolution (subgrid #1). The sizes of the pixels in the figure correspond to the sizes of grid cells in the different subgrids and reflect their relative levels of resolution. In each case the high mass density in the inner regions of the clusters results in a “burned out” image, but in the outer regions of the clusters it is clear that there are many smaller galaxy-sized mass concentrations. (There are also smaller galaxy-sized mass concentrations in the inner regions of the cluster which are not visible in Fig. 1 due to the level of contrast. See §4.6.) The bottom panels in Fig. 1 show a comparison of the mass density along the line of sight in the high- and low-resolution subgrids. Specifically, the grey-scale indicates the logarithm of the ratio of the mass density in subgrid #2 to the mass density in subgrid #1. The comparison is done at the same (low) resolution as subgrid #1. Overall the comparison is excellent (i.e. the image is fairly flat at a moderate level of grey, indicating a density ratio of order unity). The largest discrepancy between the densities in the two subgrids occurs near the “edges” of the clusters where the density in subgrid #2 is less than in the corresponding regions of subgrid #1 (i.e. white pixels). The discrepancy is caused by the relative levels of numerical softening in the two subgrids, the force being softer on a larger scale in subgrid #1 than in subgrid #2, resulting in less concentrated structure in subgrid #1 compared to subgrid #2. That is, in the outer regions of the cluster the high-resolution version is somewhat less dense than the low-resolution version since, on the whole, the cluster is more condensed in subgrid #2 than it is in subgrid #1. Spherically-averaged density profiles of the clusters computed using the two different subgrids are, however, in excellent agreement at large radii (see Fig. 5).

4. RESULTS

4.1 Mass Accretion

The growth of each of the clusters was investigated through: [1] the mean infall distance of particles into the cluster, [2] the time evolution of the total mass of the cluster contained within the Abell radius and [3] the rate at which mass was accreted within the Abell radius as a function of time. In order to calculate each of these quantities the center of mass of each cluster is required. This was determined using the following iterative procedure. Starting with an initial center of mass given by the location of the corresponding peak in the smoothed mass density field of the top grid, all subgrid particles within a radius of $3.0h^{-1}\text{Mpc}$ were selected and the center of mass of those particles was computed. From this center of mass a new sphere of particles of radius $3.0h^{-1}\text{Mpc}$ was selected and a new center of mass computed. The process was repeated within a given subgrid until convergence was reached (of order 6 iterations). Note that the centers of mass for each cluster computed independently from the corresponding high- and low-resolution subgrids are identical. Also, over the course of the simulations the centers of mass of the clusters have low streaming velocities and they move total distances which are less than the mesh resolution of the top grid.

Fig. 2 summarizes both the mean and maximum infall distances of particles over the course of the simulations. The points with error bars in Fig. 2 indicate the mean initial

distance of subgrid #1 particles from the centers of mass of their respective clusters as a function of their distance from the cluster centers of mass at the end of the simulation. That is, the points indicate the mean streaming distance of particles present in the clusters at the end of the simulation as function of their distance from the center of mass at the final timestep. The error bars show one standard deviation. The open squares without error bars indicate the *maximum* initial distance of any one particle from the center of mass of its cluster versus its distance from that cluster at the end of the simulation. From this figure, then, over the course of the simulations the mean distance traveled by particles found within the Abell radii at the end of the simulations is of order $12h^{-1}\text{Mpc}$. This is not at all surprising since the mass of the clusters within the Abell radius at $\sigma_8 = 1.0$ is of order $2 \times 10^{15}h^{-1}M_\odot$, equal to the mass contained within a uniform critical density sphere of radius $12h^{-1}\text{Mpc}$. The maximum infall distance, however, is of order $18h^{-1}\text{Mpc}$. Thus, in order to follow all of the infall of mass into the clusters over the course of the entire simulation, a simulation that utilizes either constrained initial conditions or the excision of peaks from a large-scale structure simulation would require a volume of $\sim 3 \times 10^4h^{-3}\text{Mpc}^3$ to be simulated at comparably high resolution. This is a factor of order 50 larger than the requisite volume for the highest resolution subgrid in the HPM calculation.

The masses of the clusters contained within the Abell radius, $M(r = 1.5h^{-1}\text{Mpc})$, and the rates at which mass was accreted within the Abell radius, $\dot{M}(r = 1.5h^{-1}\text{Mpc})$, were computed as a function of lookback time for each of the three clusters. The high-resolution subgrid particles were used for these calculations and the lookback time was computed by taking $\sigma_8 = 1.0$ to be the present epoch. Results for the evolution of the total amount of mass within the Abell radius, normalized by the present-day mass of the cluster within the same (comoving) distance, are shown in Fig. 3. It is clear from this figure that the details of the evolution of the clusters are somewhat different in each case but that all three gained of order 50% of their present-day mass within the past 5 to 8 Gyr. The details of the *rate* at which mass was accreted within the Abell radius are shown in Fig. 4. Here the rate at which mass was accreted by each cluster, \dot{M} , is shown as a function of lookback time and redshift, normalized by $\langle \dot{M} \rangle$, the average rate at which the cluster accreted mass between $z = 2$ and $z = 0$. From this figure it is clear that, although all three clusters have similar masses at the present, no single pattern of mass accretion dominates in the formation of the clusters. Cluster 1 shows a monotonic increase in mass accretion rate from $z = 2$ to $z = 0.2$, after which it accretes virtually no mass. Cluster 2, however, shows a monotonic decrease in the mass accretion rate from $z = 2$ to the present and cluster 3 forms via a mass accretion rate which is roughly constant.

4.3 Density Profiles

Spherically-averaged differential density profiles, $\rho(r)$, are shown in Fig. 5 for each of the clusters at the end of the simulations. Squares indicate the density profiles obtained using the high-resolution subgrid particles and triangles indicate the density profiles obtained using the low-resolution subgrid particles. Due to the numerical softening of the force on small scales the density is computed only on scales larger than two grid cells ($65h^{-1}$ kpc in the high-resolution subgrids and $260h^{-1}$ kpc in the low-resolution subgrids). Over the length scales for which the density can be computed in both the high- and low-resolution

subgrids there is excellent agreement between the two calculations and the small-scale density profile computed from the high-resolution subgrid is clearly a smooth continuation of the larger-scale density profile computed from the low-resolution subgrid. Also, but for a suggestion of a flattening in the density profile of cluster 1, there is no turnover in the density profiles at small radii, which is as expected in purely dissipationless simulations. The apparent flattening in the density profile of cluster 1 may be partially numerical in origin as it occurs on scales corresponding to 3 grid cells and less. A higher resolution simulation (eg. a third subgrid) would be required to determine whether the trend is indeed real or purely an artifact. A comparison of these density profiles and corresponding density profiles obtained from the particles in the top grid calculation is not warranted owing to the extremely poor resolution of the clusters in the top grid (of order 1000 particles in total and a force softer than Newtonian on scales smaller than the Abell radius).

It is clear from Fig. 5 that the density profiles of the clusters are not well-fit by a single power law over all scales. This is to be expected since it has been shown previously that CDM halos are well-described by density profiles in which the logarithmic slope varies gently (eg. Dubinski & Carlberg 1991; Navarro, Frenk & White 1995, 1996ab; Cole & Lacey 1996; and Tormen, Bouchet & White 1997). On scales $r \leq r_{200}$, where r_{200} is the radius inside which the mean interior overdensity is 200, a good two-parameter fit to the density profile is given by

$$\frac{\rho(r)}{\rho_c} = \frac{\delta_c}{x(1+x)^2} \quad (2)$$

(eg. Navarro, Frenk, & White 1996b) where ρ_c is the critical density for closure of the universe, $x \equiv r/r_s$, and r_s is a scale radius. Here δ_c is a dimensionless characteristic density. By defining the ‘‘concentration’’ of a halo to be $c \equiv r_{200}/r_s$, the two-parameter fit above can be reduced to a one-parameter fit through

$$\delta_c = \frac{200}{3} \frac{c^3}{[\ln(1+c) - c/(1+c)]} \quad (3)$$

(eg. Navarro, Frenk & White 1996b).

Using the particles in the highest resolution subgrids, the values of r_{200} (the ‘‘virial radius’’) for the clusters were determined at $\sigma_8 = 0.67, 0.83, 1.0$. The virial radii evolve relatively little from $\sigma_8 = 0.67$ to $\sigma_8 = 1.0$ and are of order $2h^{-1}$ Mpc for each of the clusters (see Tables 1, 2, and 3 for specific values). Again using the particles in the highest resolution subgrids, the variation of the cluster overdensities with radius were evaluated on scales less than r_{200} and results are shown by the points in Fig. 6. The solid lines in this figure illustrate the best-fitting density profiles of the form of equation (3) above. The values of the corresponding scale radii, r_s , are given in each of the panels of the figure. But for a slight downturn in the small-scale density profiles of cluster 2 at $\sigma_8 = 0.67$ and cluster 3 at $\sigma_8 = 0.83$, there is very good agreement between the simulated clusters and equation (3). Again, it is possible that the small-scale downturn is numerical in origin. The scaled density profiles in Fig. 6 are all fairly similar and in the case of clusters 1 and 2 the scale radius of the best-fitting profile evolves little from $\sigma_8 = 0.67$ to $\sigma_8 = 1.0$; however, for cluster 3 the value of r_s changes appreciably (by a factor of order 2) over the same time period.

4.4 3-d Shapes & 2-d Ellipticity Distributions

The evolution of the 3-dimensional and projected shapes of the clusters were computed at $\sigma_8 = 0.67, 0.83,$ and 1.0 using the particles in the highest resolution subgrids. Since there is no hard “edge” to the clusters in terms of distinguishing those particles which are inside the cluster and those which are not, we shall define the boundaries of the clusters to be the virial radii (r_{200}) for the following analyses.

Using all particles within r_{200} of the cluster centers of mass, the 3-dimensional cluster shapes were determined from a standard moment of inertia analysis that yielded the axis ratios b/a and c/a for each of the clusters (we define $a > b > c$). From the axial ratios a triaxiality parameter was computed for each of the clusters:

$$T = \frac{a^2 - b^2}{a^2 - c^2} \quad (4)$$

where $T = 0$ indicates a purely oblate object and $T = 1$ indicates a purely prolate object. We shall refer to objects with $0 < T < 1/3$ as being nearly oblate, those with $2/3 < T < 1$ as nearly prolate, and those with $1/3 < T < 2/3$ as triaxial. Values of the cluster axial ratios and triaxiality parameters are listed in Tables 1, 2, and 3 for σ_8 between 0.67 and 1.0. From these tables it is clear that the evolution of the shapes of the clusters are quite different in each case. Although cluster 1 and cluster 2 are both nearly oblate at the end of the simulation, cluster 1 evolves from being triaxial at $\sigma_8 = 0.67$ to being nearly oblate at $\sigma_8 = 1.0$ whereas the shape of cluster 2 changes little over the same period of time and, as a result, is always nearly oblate. Cluster 3, on the other hand, is nearly prolate at the end of the simulation but was nearly oblate at $\sigma_8 = 0.67$.

A more useful quantity for comparison of the evolution of the shapes of simulated clusters to observed clusters is the ellipticity projected on the plane of the sky. In the case of the simulations the projected ellipticity of the mass is the only quantity which can be computed reliably (i.e. without having to resort to assumptions about the degree to which mass would trace light). Given recent advances in gravitational lensing analyses of observed clusters, however, this seems a reasonable quantity to compute. That is, from analyses of the coherent weak distortion of the shapes of background galaxies due to an intervening gravitational lens cluster it is possible to constrain the ellipticity of the projected mass of clusters and, additionally, it is becoming clear that the smoothed light distribution of clusters traces the mass quite well (eg. Bonnet, Mellier & Fort 1994; Fahlman et al. 1994; Smail et al. 1995; Kneib et al. 1996; Seitz et al. 1996; Squires et al. 1996ab; Smail et al. 1997).

The ellipticities of the clusters as projected on the sky, $\epsilon = 1 - b/a$, were computed using all particles in the the highest resolution subgrids that were located within a distance of r_{200} of the cluster centers of mass. The probability, $P(\epsilon)$, of observing a given projected ellipticity for a given cluster was computed by viewing each cluster from 500 random orientations and assembling an appropriately normalized probability distribution function. Results are shown in Fig. 7 for all 3 clusters at $\sigma_8 = 0.67, 0.83,$ and 1.0 . Again, as with the evolution of the triaxiality parameter, each cluster exhibits its own particular evolution in projected shape. Cluster 1 evolves toward being, on average, significantly flatter in projection at $\sigma_8 = 1.0$ than it was at $\sigma_8 = 0.67$. Cluster 2, on the other hand, remains

approximately the same projected shape over the same time period and cluster 3 evolves toward being significantly rounder in projection on average. The median ellipticities for each of the clusters, ϵ_{med} , are listed in Tables 1, 2, and 3.

4.5 Substructure

The redshift dependence of the fraction of observed clusters having a significant amount of substructure is potentially a good indicator of the value of density parameter. This is due to the fact that in a universe in which $\Omega_0 \leq 1$ density fluctuations cease to grow at redshifts of order $\Omega_0^{-1} - 1$ and, so, moderate to low redshift clusters in critical density universes are expected to contain substantial amounts of substructure on average while in low density universes the clusters should be much more regular. Wilson, Cole & Frenk (1996) have explored the possibility of using observations of weak lensing by clusters to discriminate between universes with low and critical values of Ω_0 via a quantification of cluster substructure from the weak shear field. Although initially optimistic, the situation has become more murky recently with the realization that some of the simulated clusters used in the analysis were inadequate.

The simulations discussed here are restricted to a critical density universe and, hence, we do not investigate the explicit Ω_0 dependence of cluster substructure with cosmological epoch (this analysis will be performed in future simulations). Rather, we have investigated the evolution of substructure in the clusters from $\sigma_8 = 0.67$ to $\sigma_8 = 1.0$ in order to assess the degree to which substructure is erased over this period of time.

There are numerous methods by which cluster substructure can be quantified but here we restrict the analysis to the Dressler-Shectman Δ statistic (Dressler & Shectman 1988). This choice is made based on the results of Pinkey et al. (1996) who have subjected many substructure tests to thorough analysis and conclude that by and large the Dressler-Shectman test tends to be the most sensitive to substructure.

The Δ statistic is defined by

$$\Delta = \frac{1}{N} \sum_{i=1}^N \delta_i, \quad \delta_i^2 = \frac{N_{\text{loc}}}{\sigma^2} \left[(\bar{v}_i - \bar{v})^2 + (\sigma_i - \sigma)^2 \right] \quad (5)$$

where N is the number of galaxies in the cluster and \bar{v}_i and σ_i are, respectively, the mean velocity and the velocity dispersion of the N_{loc} nearest neighbors to each galaxy. The sensitivity of the Δ statistic is dependent upon the number of neighboring galaxies used in the analysis and Bird (1995) finds the test to be most sensitive for $N_{\text{loc}} = \sqrt{N}$. The statistic is a measure of the correlation between the (projected) locations of the galaxies in the cluster and their velocities. In the case of uncorrelated positions and velocities $\Delta \sim 1$. The quantification of substructure for a given cluster using only the computed value of Δ is insufficient, however, and in order to assess the likelihood of real substructure within the cluster Monte Carlo simulations must be performed. Additionally, Crone, Evrard & Richstone (1996) have pointed out that since the value of Δ is not independent of N , the total number of galaxies used in the analysis, in order to compare either observed or theoretical clusters to one another it is necessary in the analyses to select an identical number of galaxies for each cluster.

The simulations presented here are of insufficient resolution to resolve the dark matter halos of individual galaxies (see §4.6 below) and we instead investigate the substructure in the mass distribution. (For all intents and purposes this is the nature of the substructure identified via weak lensing, though there is clearly good correspondence between “lumpiness” in the mass and galaxy distributions in lensing clusters.) Substructure in the clusters was evaluated in the following way. Since the specific value of Δ for a given cluster will depend on the angle from which it is viewed in projection, each cluster was viewed from 500 random directions. For each viewing angle, the projected locations of a randomly selected subset of the particles was used to compute a value of Δ . Additionally, for each viewing angle a Monte Carlo value of the statistic (Δ_{rand}) was computed by randomly shuffling the velocities of the particles amongst their positions. Mean values of Δ and Δ_{rand} , along with their formal standard deviations, were then computed from the 500 individual values. For each cluster a total of $N = 1024$ particles were randomly selected from all particles within the virial radius (r_{200}). Different random sets of particles were used for each viewing angle and for the timesteps corresponding to $\sigma_8 = 0.67$, 0.83 , and 1.0 . Following Bird (1995), N_{loc} was taken to be $\sqrt{N} = 32$.

Tables 1, 2, and 3 list the mean values of the Δ statistic for each cluster computed from the 500 random viewing angles, the mean values computed from the 500 Monte Carlo position-velocity shuffles (Δ_{rand}), and the corresponding $1\text{-}\sigma$ errors. Also listed are the ratios $\Delta/\Delta_{\text{rand}}$, which indicate that all three clusters contain significant amounts of substructure at each of the three epochs, σ_8 . That is, within the virial radius substructure in the mass distribution of the clusters is not completely erased by the end of the simulation. In the case of cluster 2, the degree of substructure over and above the expectations of random is roughly constant at a $\sim 3\text{-}\sigma$ level from $\sigma_8 = 0.67$ to $\sigma_8 = 1.0$. In the case of clusters 1 and 3, there is significantly less substructure at $\sigma_8 = 1.0$ than at $\sigma_8 = 0.67$. However, the “erasure” of substructure in these two clusters over this time period is not quite monotonic. Cluster 1 is a bit “lumpier” at $\sigma_8 = 0.83$ than it is at either $\sigma_8 = 0.67$ or $\sigma_8 = 1.0$, while cluster 2 is a bit smoother and less “lumpy” at $\sigma_8 = 0.83$ than it is at either $\sigma_8 = 0.67$ or $\sigma_8 = 1.0$.

Bubble plots of the Δ test are very helpful for illustrating visually both the location and amount substructure in a cluster. Fig. 8 shows bubble plots for each of the clusters at the end of the simulation. The viewing angle for the projection of each cluster was chosen to be an angle for which the specific value of Δ was identical to the mean value of the 500 random orientations. The dots in Fig. 8 show the spatial locations of the 1024 randomly selected mass points used in the Δ statistic analysis. The circles, all of which are centered on dots, have been scaled to have radii proportional to δ_i (see equation 5 above). The larger the circle, the larger is the local deviation of the mean velocity and/or velocity dispersion from the global cluster value. For clarity, circles are drawn around only those mass points for which $\delta_i > 2\Delta$ (i.e. regions of most significant substructure). Far from being smooth blobs of mass, the clusters are all clearly “lumpy”, each having of order 4 or 5 significant sub-lumps within the virial radius.

4.6 Galaxy Halos

It is often thought, erroneously, that purely dissipationless simulations are inadequate to study the dark matter halos of galaxies in a simulated cluster environment because all

small dark matter concentrations are destroyed by purely numerical effects as they orbit through the cluster. However, Bromley et al. (1995) have demonstrated that provided the force resolution is high galaxy-sized dark matter halos will survive many orbits through the potential of a large cluster and are not destroyed by purely numerical effects.

In the case of this work, the study of individual galaxy-sized dark halos in the clusters is not a reasonable goal since the length scale over which the force is non-Newtonian is somewhat too large, even in the case of the highest resolution subgrids. However, it can be seen in Fig. 1 that there are numerous galaxy-sized concentrations of dark matter in the outer regions of the clusters and the clusters are not merely smooth blobs of mass. (The lumpiness of the mass distribution is borne out in part by the substructure analysis above.) Due to the high particle density in the central regions and the choice of contrast level, existing galaxy-sized concentrations in the inner regions of the clusters are not visible in Fig. 1.

Although it is clearly an inadequate method for the generation of a highly accurate catalog of galaxy-sized dark halos, a simple friends-of-friends algorithm was used to generate catalogs of groups of particles in the highest resolution subgrids. The groups were selected to have overdensities $\delta \gtrsim 1000$ (typical of the overdensity of the luminous region of a bright galaxy) and masses $\gtrsim 10^{11}h^{-1}M_{\odot}$ (20 particles or more). At the end of the simulations, ~ 300 such objects were found within the Abell radii of clusters 1 and 3, and ~ 200 were found within the Abell radius of cluster 2. However, owing to the large scale over which the force is softer than Newtonian, the central $0.5h^{-1}\text{Mpc}$ of each cluster is dominated by a single huge “halo” of mass $\sim 10^{15}h^{-1}M_{\odot}$.

By nesting yet another subgrid within the highest resolution subgrid (i.e. by performing a 4-level calculation), the effective length scale over which the force is softer than Newtonian will be reduced significantly. Within the Abell radius of a cluster it will then be possible to resolve confidently groups of particles that may be fairly associated with the dark matter halos of individual galaxies and to eliminate the artificial overmerging of halos in the central region. Such analyses will be performed in future simulations.

5. DISCUSSION

Using a hybrid N-body code in which high mass and spatial resolution can be obtained in small regions of a very large total simulation volume, the formation of three massive clusters was investigated. The clusters were chosen to be typical of the most massive clusters that would be present in a standard CDM universe at an epoch corresponding to $\sigma_8 = 1.0$. At highest resolution, the clusters consisted of $\sim 4 \times 10^5$ particles within the Abell radius at $\sigma_8 = 1.0$. Although the clusters share similar properties at the end of the simulation, the details of their formation histories are quite different.

The properties which the clusters share are:

- formation within the same large computational volume (200^3h^{-3}Mpc^3)
- masses of $M(r \leq 1.5h^{-1}\text{Mpc}) \sim 2 \times 10^{15}h^{-1}M_{\odot}$ at the end of the simulation
- similar spherically-averaged density profiles which are well-fit by equation (2)
- similar values of the virial radius, r_{200} , and similar values of the scale radius, r_s , at the end of the simulation

- accretion of $\sim 50\%$ of the mass present at the end of the simulation within the past 5 to 8 Gyr

In terms of the details of the formation history of the clusters, however, each cluster exhibits markedly individual behavior and no single pattern dominates in the evolution of the following cluster properties:

- mass accretion rate, \dot{M}
- scale radius, r_s
- three-dimensional shape (triaxiality parameter, T)
- two-dimensional (projected) ellipticity
- substructure (Dressler-Shectman Δ statistic)

Based on the very small number of clusters presented here it is difficult to make any statistically-sound conclusions about cluster formation and evolution. However, the problems with standard CDM notwithstanding, there are certainly some interesting things to be noted. The numerical clusters are extremely massive and, so, correspond to rich clusters. Rich clusters, being the brightest and most massive, are likely to be those which will be studied observationally over the widest range of redshifts and are the objects from which it is hoped that cosmological constraints will arise. Given the markedly different formation histories of the clusters, a question raised by this investigation is the degree to which observations of a sample of rich clusters covering a wide range of redshifts can provide stringent cosmological constraints.

Although the numerical clusters studied here do not constitute a statistically large sample, it is clear that such large clusters do not form a simple 1-parameter family as far as their evolution history is concerned, even though the clusters have similar masses and spherically-averaged density profiles at the present day. The use of observations of cluster evolution to constrain cosmological models may yet be viable but the cautious suggestion from this work is that this may not be completely straightforward. Considerably more work on the details of the formation history of clusters in various models of structure formation is necessary in order to determine both the degree to which cosmological conclusions can be drawn from observations of clusters at different epochs and also the requisite size of a sample of observed clusters which would insure those cosmological conclusions to be statistically reliable.

ACKNOWLEDGMENTS

Generous amounts of CPU time on the Cray J-90 at the Max-Planck-Institut für Astrophysik and enlightening conversations with Simon White are gratefully acknowledged. This work was supported in part by the NSF under contract AST-9616968.

REFERENCES

- Bahcall, N. A. & Cen, R. 1993, ApJ, 407, L49
 Bartelmann, M., Ehlers, J. & Schneider, P. 1993, A&A, 280, 351
 Beers, T. C. & Geller, M. J. 1983, ApJ, 274, 491

Bird, C. M. 1994a, ApJ, 422, 480
 Bird, C. M. 1994b AJ, 107, 1637
 Bird, C. M. 1995, ApJ, 445, L81
 Bonnet, H., Mellier, Y., & Fort, B., 1994, ApJ, 427, L83
 Bower, R. G. & Smail, I. 1997, MNRAS, in press (astro-ph/9612151)
 Bromley, B. C., Warren, M. S., Zurek, W. H., & Quinn, P. J. 1995, AIP Conference Proceedings 336, 433
 Bunn, E. & White, M. 1997, ApJ, 480, 6
 Carlberg, R. G. 1994, ApJ, 433, 468
 Cole, S. M. & Lacey, C. G. 1996, MNRAS, 281, 716
 Crone, M. M., Evrard, A. E. & Richstone, D. O. 1996, ApJ, 467, 489
 Davis, D. S. & Mushotzky, R. F. 1993, AJ, 105, 409
 Deltorn, J.-M., Le Fevre, O., Crampton, D., & Dickinson, M. 1997, ApJ (Letters), in press (astro-ph/9704086)
 Dressler, A. & Shectman, S. A. 1988, AJ, 95, 985
 Dubinski, J. & Carlberg, R. 1991, ApJ, 378, 496
 Eke, V. R., Cole, S. & Frenk, C. S. 1996, MNRAS, 282, 263
 Fahlman, G., Kaiser, N., Squires, G., & Woods, D., 1994, ApJ, 437, 56
 Jones, C. & Forman, W. 1984, ApJ, 276, 38
 Kauffmann, G. & White, S. D. M. 1993, MNRAS, 261, 921
 Kneib, J-P, Ellis, R. S., Smail, I., Couch, W. J., & Sharples, R. M. 1996, ApJ, 471, 643
 Lacey, C. & Cole, S. 1993, MNRAS, 262, 627
 Luppino, G. & Kaiser, N. 1997, ApJ, 475, 20
 Miyaji, T., Mushotzky, M., Lowenstein, M., Serlemitsos, P. J., Marshall, F. E., Petre, R., Jahoda, K. M., Boldt, E. A., Holt, S. S., Swank, J., Szymkowiak, A. E., & R. Kelley 1993, ApJ, 419, 66
 Mohr, J. J., Evrard, A. E., Fabricant, D. G., & Geller, M. J. 1995, ApJ, 447, 8
 Mushotzky, R. 1993, ANYAS, 699, 184
 Navarro, J. F., Frenk, C. S. & White, S. D. M. 1995, MNRAS, 275, 720
 Navarro, J. F., Frenk, C. S. & White, S. D. M. 1996a, ApJ, 462, 563
 Navarro, J. F., Frenk, C. S. & White, S. D. M. 1996b, ApJ, submitted (astro-ph/9611107)
 Pinkey, J., Roettiger, K., Burns, J. O., & Bird, C. M. 1996, ApJS, 104, 1
 Richstone, D., Loeb, A. & Turner, E. L. 1992, ApJ, 393, 477
 Seitz, C., Kneib, J.-P., Schneider, P., & Seitz, S., 1996, A&A, 314, 707
 Smail, I. & Dickinson, M. 1995, ApJ, 455, L99
 Smail, I., Ellis, R. S., Fitchett, M. J., & Edge, A. C., 1995, MNRAS, 273, 277
 Smail, I., Ellis, R. S., Dressler, A., Couch, W. J., Oemler, A., Sharples, R., & Butcher, H. 1997, ApJ, 479, 70
 Squires, G., Kaiser, N., Babul, A., Fahlman, G., Woods, D., Neumann, D. M., & Böhringer, H. 1996a, ApJ, 461, 572
 Squires, G., Kaiser, N., Fahlman, G., Babul, A., et al., 1996b, ApJ, 469, 73
 Steidel, C., Dickinson, M., Meyer, D., Adelberger, K. & Sembach, K. 1997, ApJ, submitted (astro-ph/9610230)
 Tormen, G., Bouchet, F. & White, S. D. M. 1997, MNRAS, 286, 865

West, M. J. & Bothun, G. D. 1990, ApJ, 350, 36
 White, S. D. M., Briel, U. G. & Henry, J. P. 1993, MNRAS, 261, L8
 White, S. D. M., Efstathiou, G. & Frenk, C. S. 1993, MNRAS, 262, 1023
 Wilson, G., Cole, S. & Frenk, C. S. 1996, MNRAS, 282, 501
 Viana, T. P. & Liddle, A. R. 1996, MNRAS, 281, 323
 Villumsen, J. V. 1989, ApJS, 71, 407
 Zabludoff, A. I. & Zaritsky, D. 1995, ApJ, 447, L21

FIGURE CAPTIONS

Fig. 1a: Grey-scale images of cluster 1 at $\sigma_8 = 1.0$. The top panel shows the logarithm of the mass density along the line of sight in the high-resolution subgrid (subgrid #2) and the center panel shows the same for the low resolution subgrid (subgrid #1). The pixel sizes in the image are equal to the grid cell sizes in the subgrids and the projection is of a $8.3h^{-1}\text{Mpc} \times 8.3h^{-1}\text{Mpc} \times 8.3h^{-1}\text{Mpc}$ cube, centered on the center of mass of the cluster. The bottom panel shows a comparison of the line of sight mass density in the two subgrids, where the grey scale indicates the logarithm of the mass density in subgrid #2 divided by the mass density in subgrid #1, computed at the (low) resolution of subgrid #1. Overall, the mass density in the two subgrids compares well (see text).

Fig. 1b: Same as Fig. 1a, but for cluster 2.

Fig. 1c: Same as Fig. 1a, but for cluster 3.

Fig. 2: The infall distance of particles into the clusters. Solid points with error bars show the mean distance streamed since the beginning of the simulation as a function of the final location of the particles, computed relative to the cluster centers of mass. Error bars indicate one standard deviation. The open squares show the maximum initial distance of any one particle from the center of mass of its cluster as a function of its location at the end of the simulation.

Fig. 3: Mass of the clusters contained within the Abell radius as a function of lookback time. The contained mass has been normalized by the contained mass at the end of the simulation. All three clusters have masses $\sim 2 \times 10^{15}h^{-1}\text{Mpc}$ within the Abell radius at the end of the simulation (see Tables 1, 2, and 3).

Fig. 4: Rate at which mass is accreted, \dot{M} , within the Abell radius as a function of lookback time. The accretion rate is normalized by the mean rate, $\langle \dot{M} \rangle$, at which mass is accreted within the Abell radius between lookback times corresponding to $z = 2$ and $z = 0$.

Fig. 5: Spherically averaged density profiles for each of the clusters, evaluated at $\sigma_8 = 1.0$. Open squares indicate $\rho(r)$ computed using the high-resolution subgrid particles; filled triangles indicate $\rho(r)$ computed using the low-resolution subgrid particles.

Fig. 6: Cluster overdensities as a function of radius (scaled by r_{200} , the virial radius) for $\sigma_8 = 0.67, 0.83$ and 1.0 . Results for cluster 1 are shown in the three panels on the left, results for cluster 2 are shown in the three central panels, and results for cluster 3 are shown in the three panels on the right. The solid line indicates the best-fit density profile of the form of equation (2), with the corresponding value of the scale radius, r_s , indicated in each of the individual panels of the figure.

Fig. 7: Projected ellipticity distributions for each of the clusters as a function of σ_8 . The dashed line indicates $\sigma_8 = 0.67$, the dotted line indicates $\sigma_8 = 0.83$, and the solid line indicates $\sigma_8 = 1.0$.

Fig. 8: Bubble plots of the Δ test for each cluster at $\sigma_8 = 1.0$. The linear scale of the projection is $5h^{-1}\text{Mpc}$ by $5h^{-1}\text{Mpc}$. Dots indicate the spatial location of the mass points used in the evaluation of Δ and the circles have radii proportional to δ_i (see text). The degree of substructure apparent in these projections is indicative of the mean value, based on the results of 500 random viewing angles.

Table 1: Properties of cluster 1 (results of highest resolution subgrid)

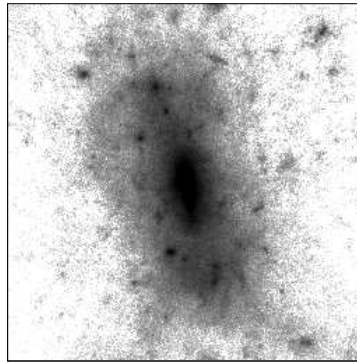
	$\sigma_8 = 0.67$	$\sigma_8 = 0.83$	$\sigma_8 = 1.0$
$M(r \leq 1.5h^{-1}\text{Mpc})$	$8.9 \times 10^{14}h^{-1}M_\odot$	$1.8 \times 10^{15}h^{-1}M_\odot$	$1.9 \times 10^{15}h^{-1}M_\odot$
$N_p(r \leq 1.5h^{-1}\text{Mpc})$	1.8×10^5	3.7×10^5	3.9×10^5
r_{200}	$1.60h^{-1}\text{Mpc}$	$2.18h^{-1}\text{Mpc}$	$2.27h^{-1}\text{Mpc}$
b/a	0.87	0.91	0.97
c/a	0.76	0.76	0.68
T	0.60	0.38	0.12
ϵ_{med}	0.30	0.27	0.38
Δ	1.75 ± 0.12	1.86 ± 0.12	1.30 ± 0.09
Δ_{rand}	1.05 ± 0.07	0.97 ± 0.07	1.04 ± 0.07
$\Delta/\Delta_{\text{rand}}$	1.67 ± 0.16	1.92 ± 0.18	1.25 ± 0.12

Table 2: Properties of cluster 2 (results of highest resolution subgrid)

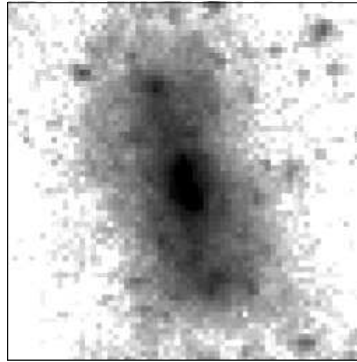
	$\sigma_8 = 0.67$	$\sigma_8 = 0.83$	$\sigma_8 = 1.0$
$M(r \leq 1.5h^{-1}\text{Mpc})$	$1.2 \times 10^{15}h^{-1}M_\odot$	$1.5 \times 10^{15}h^{-1}M_\odot$	$1.7 \times 10^{15}h^{-1}M_\odot$
$N_p(r \leq 1.5h^{-1}\text{Mpc})$	2.4×10^5	3.0×10^5	3.5×10^5
r_{200}	$1.83h^{-1}\text{Mpc}$	$2.05h^{-1}\text{Mpc}$	$2.08h^{-1}\text{Mpc}$
b/a	0.98	0.98	0.97
c/a	0.76	0.76	0.79
T	0.10	0.08	0.15
ϵ_{med}	0.30	0.30	0.26
Δ	1.45 ± 0.10	1.43 ± 0.10	1.49 ± 0.10
Δ_{rand}	1.06 ± 0.08	1.06 ± 0.07	1.07 ± 0.07
$\Delta/\Delta_{\text{rand}}$	1.38 ± 0.14	1.35 ± 0.13	1.39 ± 0.13

Table 3: Properties of cluster 3 (results of highest resolution subgrid)

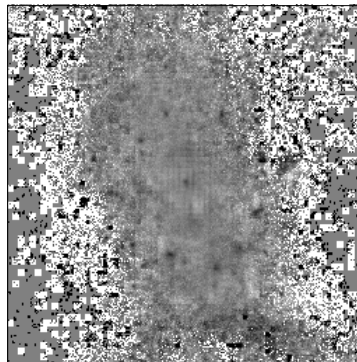
	$\sigma_8 = 0.67$	$\sigma_8 = 0.83$	$\sigma_8 = 1.0$
$M(r \leq 1.5h^{-1}\text{Mpc})$	$1.2 \times 10^{15}h^{-1}M_\odot$	$1.5 \times 10^{15}h^{-1}M_\odot$	$2.1 \times 10^{15}h^{-1}M_\odot$
$N_p(r \leq 1.5h^{-1}\text{Mpc})$	2.4×10^5	3.0×10^5	4.3×10^5
r_{200}	$1.87h^{-1}\text{Mpc}$	$2.06h^{-1}\text{Mpc}$	$2.24h^{-1}\text{Mpc}$
b/a	0.96	0.94	0.87
c/a	0.70	0.77	0.86
T	0.16	0.31	0.93
ϵ_{med}	0.30	0.30	0.21
Δ	1.76 ± 0.12	1.39 ± 0.09	1.48 ± 0.09
Δ_{rand}	1.02 ± 0.06	1.08 ± 0.07	1.06 ± 0.07
$\Delta/\Delta_{\text{rand}}$	1.72 ± 0.15	1.29 ± 0.12	1.40 ± 0.12



Subgrid #2



Subgrid #1



Subgrid #2 - Subgrid #1

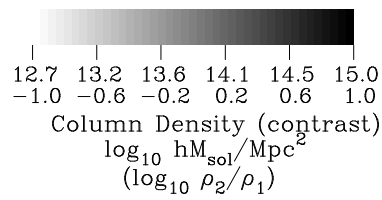
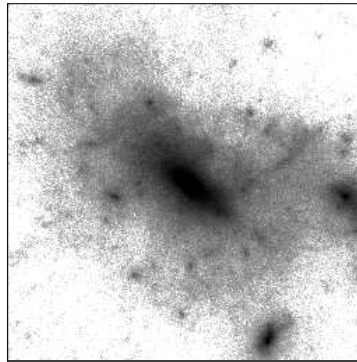
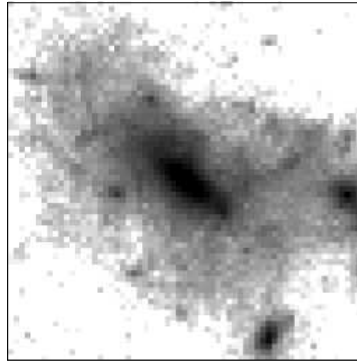


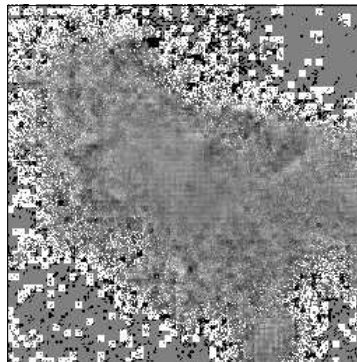
Figure 1a



Subgrid #2



Subgrid #1



Subgrid #2 - Subgrid #1

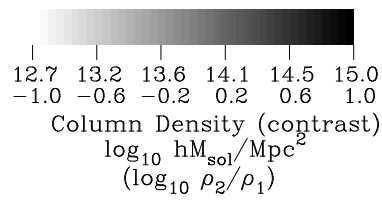
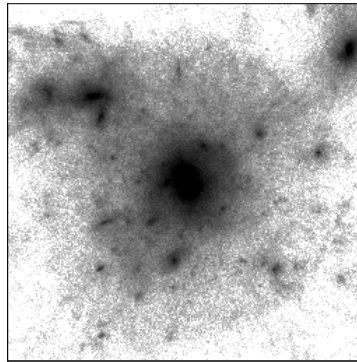
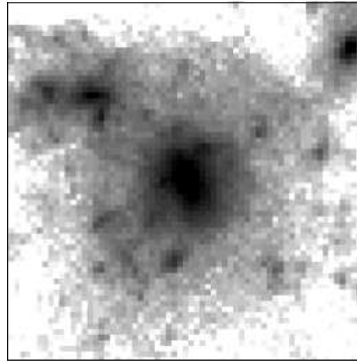


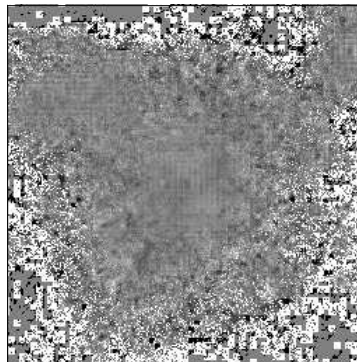
Figure 1b



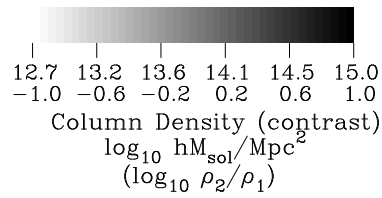
Subgrid #2



Subgrid #1



Subgrid #2 - Subgrid #1



Column Density (contrast)
 $\log_{10} hM_{\text{sol}}/\text{Mpc}^2$
 $(\log_{10} \rho_2/\rho_1)$

Figure 1c

Figure 2

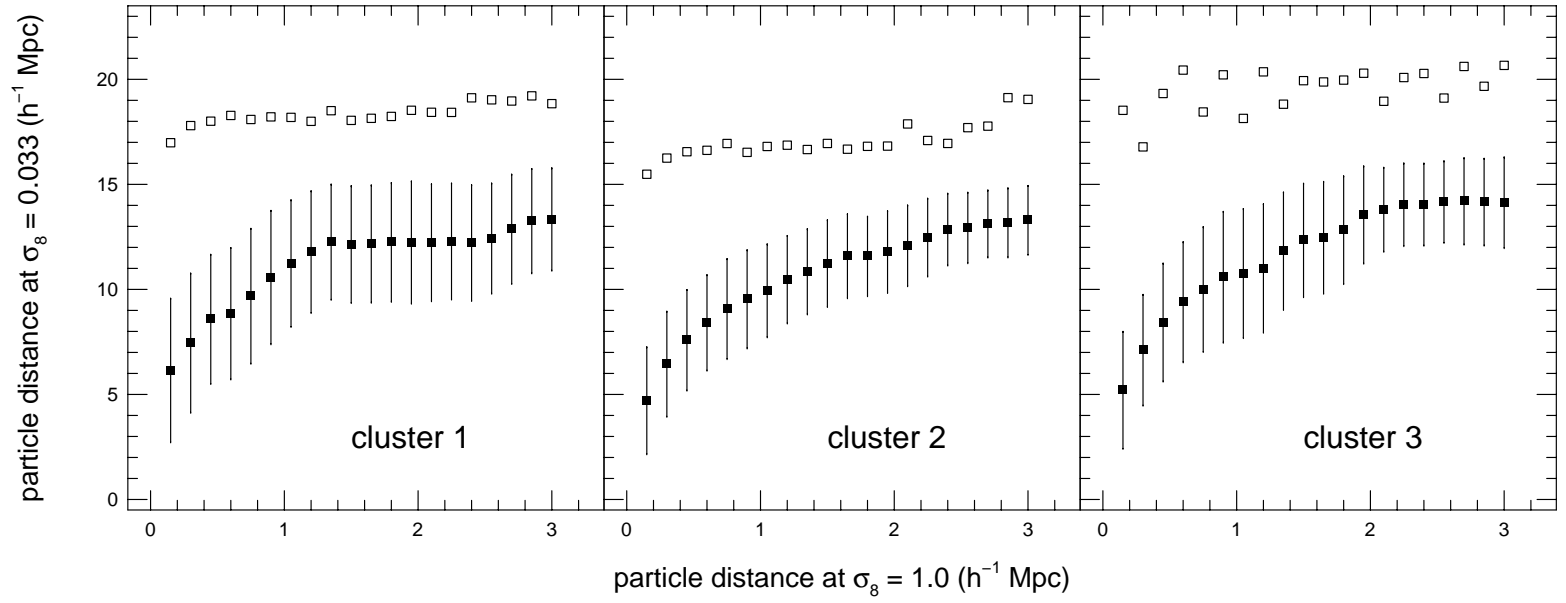


Figure 3

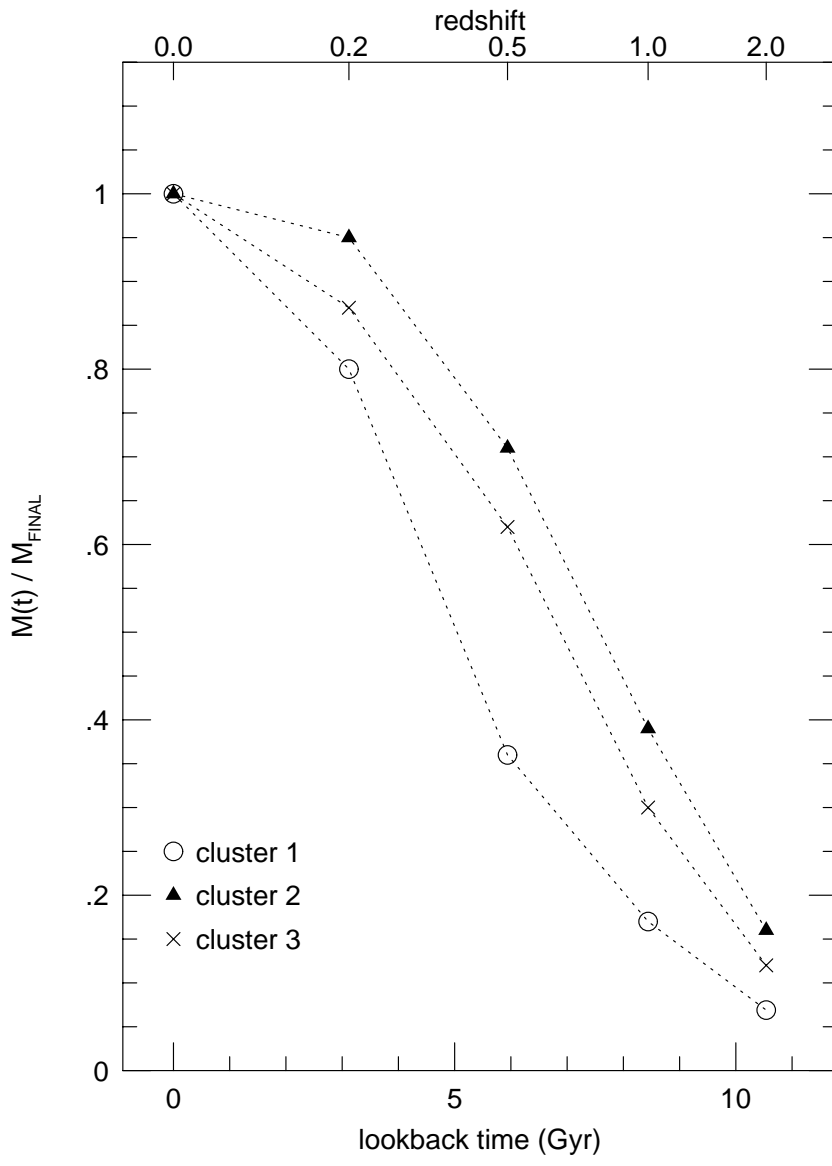


Figure 4

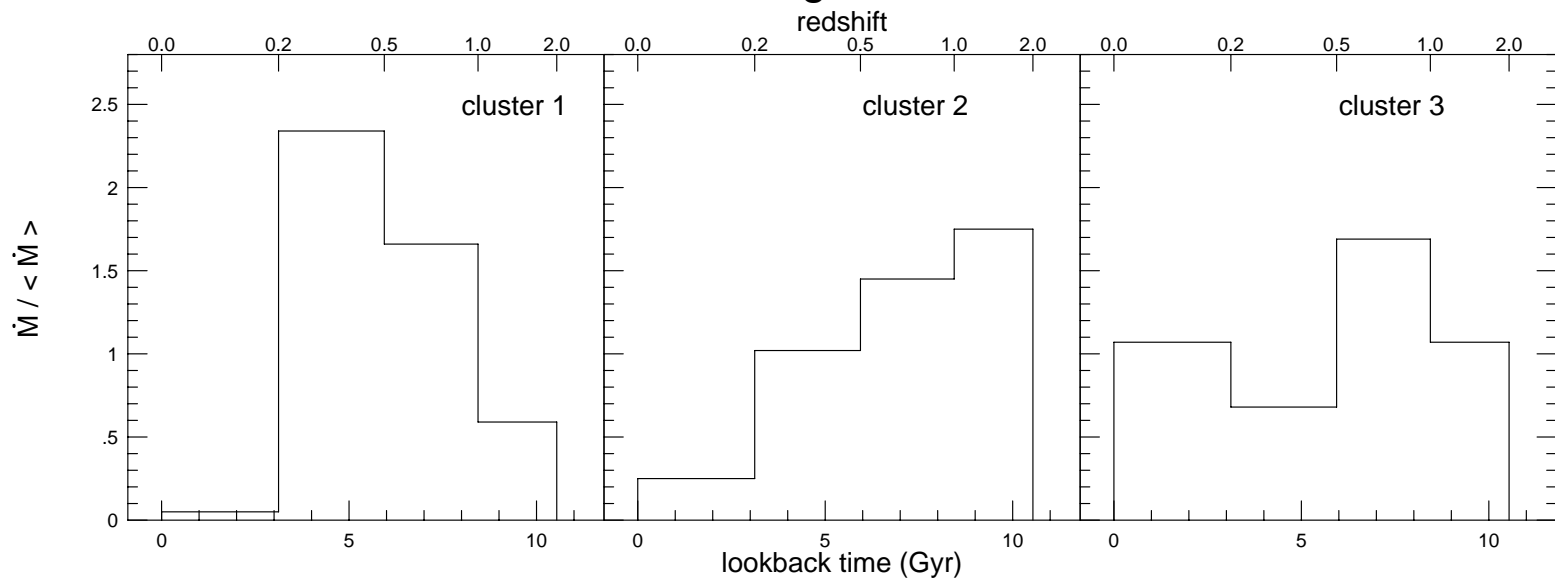


Figure 5

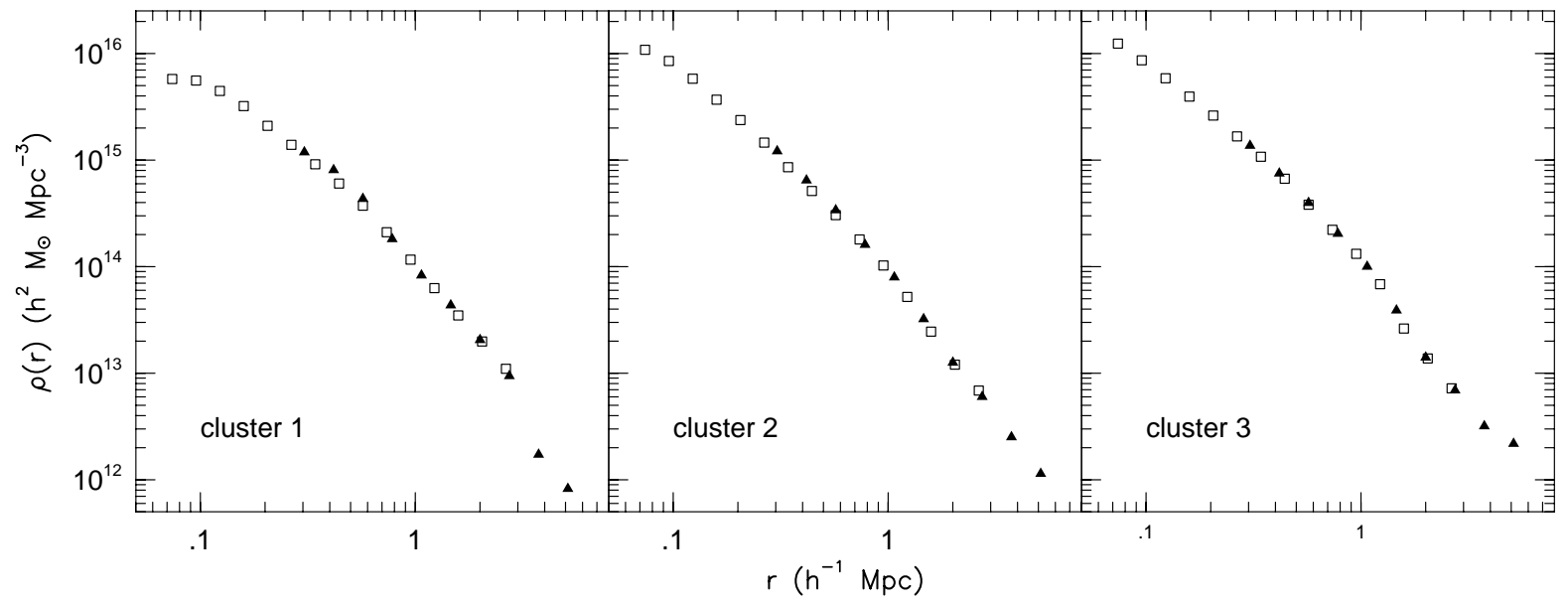


Figure 6

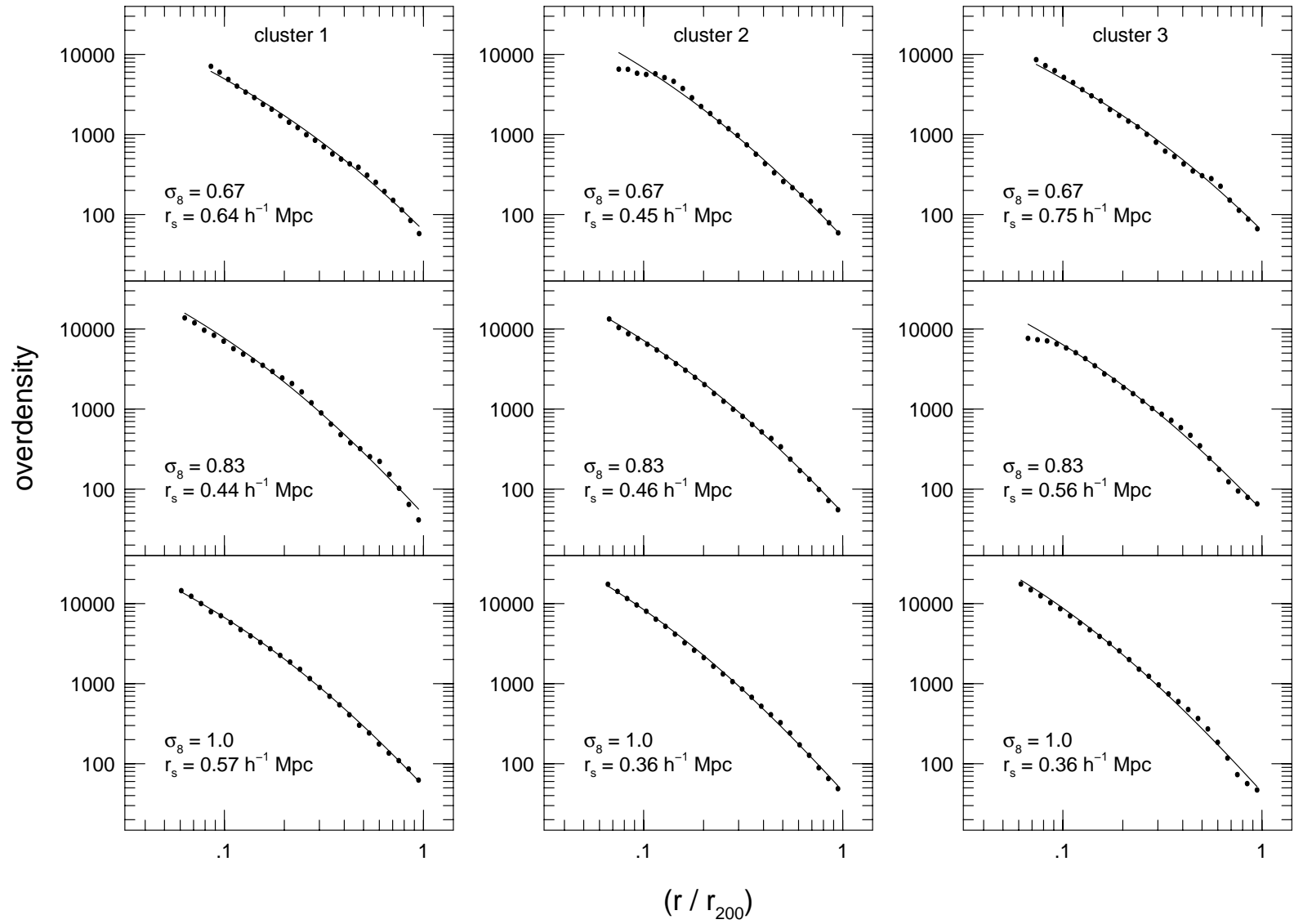


Figure 7

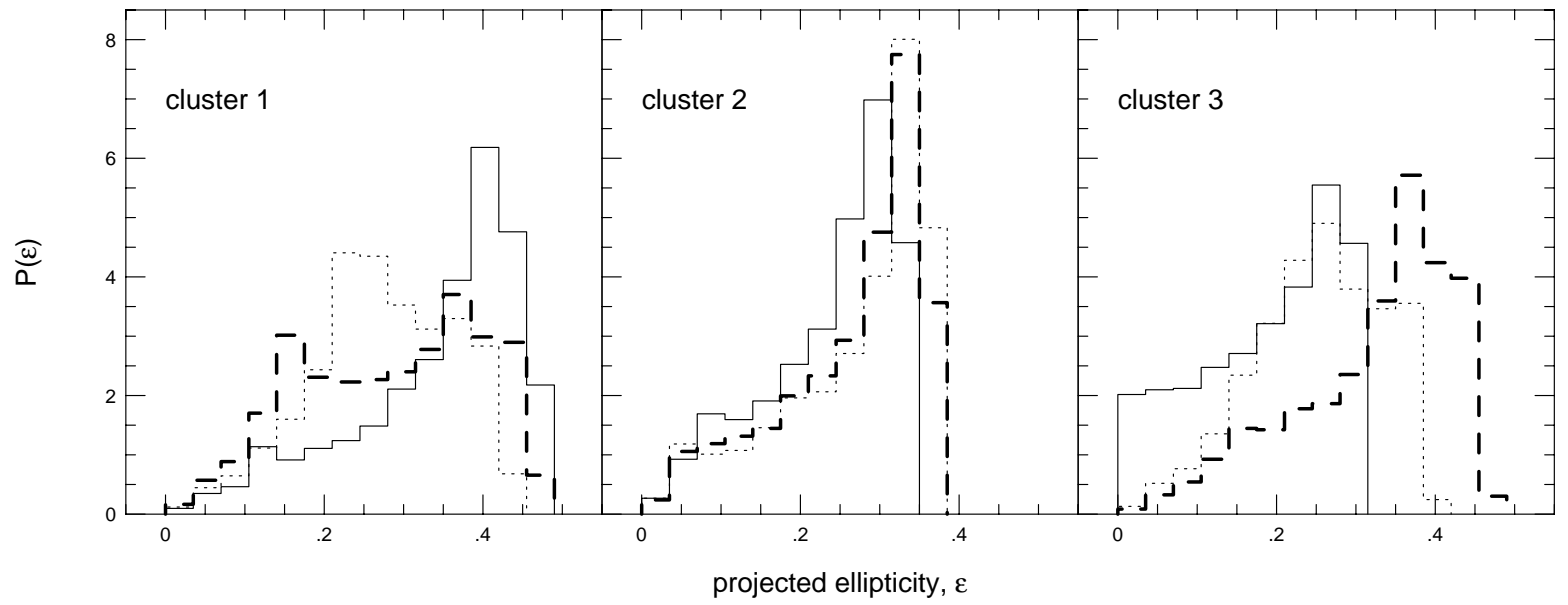


Figure 8

